Revisiting Metal Fluorides as Lithium-ion Battery Cathodes

Xiao Hua[1,2,3], Alexander S. Eggeman[4,5], Elizabeth Castillo-Martínez[1,6], Rosa Robert[1], Harry S. Geddes[3], Ziheng Lu[4], Chris J. Pickard[4,7], Wei Meng[1], Kamila M. Wiaderek[8], Nathalie Pereira[9], Glenn G. Amatucci[9], Paul A. Midgley[4], Karena W. Chapman[8,10], Ullrich Steiner[2], Andrew L. Goodwin[3], and Clare P. Grey[1*]*

1: Department of Chemistry, University of Cambridge, Lensfield Road, Cambridge, CB2 1EW, United Kingdom

2: Adolphe Merkle Institute, Chemin des Verdiers 4, 1700 Fribourg, Switzerland

3: Inorganic Chemistry Laboratory, University of Oxford, South Parks Road, Oxford OX1 3QR, United Kingdom

4: Department of Materials Science and Metallurgy, University of Cambridge, Pembroke Street, Cambridge CB2 3QZ, United Kingdom

5: Department of Materials, University of Manchester, Manchester M13 9PL, United Kingdom

6. Departamento Química Inorgánica, Universidad Complutense de Madrid, 28040 Madrid, Spain

7: Advanced Institute for Materials Research, Tohoku University, Sendai, Japan

8: X-ray Science Division, Advanced Photon Source, Argonne National Laboratory, Argonne, Illinois 60439, United States

9: Energy Storage Research Group, Department of Materials Science and Engineering, Rutgers University, North Brunswick, New Jersey 08902, United States

10: Department of Chemistry, SUNY Stony Brook, Stony Brook, NY 11790-3400, United States

ABSTRACT

Metal fluorides, promising lithium-ion battery cathode materials, have been classified as conversion materials, due to the reconstructive phase transitions widely presumed to occur upon lithiation. We challenge this view by studying FeF_3 using X-ray total scattering and electron diffraction techniques that measure structure over multiple length-scales coupled with DFT calculations, and by revisiting prior experimental studies of FeF_2 and CuF_2. Metal fluoride lithiation is instead dominated by diffusion-controlled displacement mechanisms, a clear topological relationship between the metal fluoride F^- sublattices and that of LiF being established. Initial lithiation of FeF_3 forms FeF_2 on the particle's surface, along with a cation- and stacking-disordered phase, *A*-$Li_xFe_yF_3$ – structurally related to *α*-/*β*-$LiMn^{2+}Fe^{3+}F_6$, which topotactically transforms to *B*- and then *C*-$Li_xFe_yF_3$, before forming LiF and Fe. Lithiation of FeF_2 and CuF_2 results in a buffer phase between FeF_2/CuF_2 and LiF. The resulting principles will aid future developments of a wider range of isomorphic metal fluorides.

In the search for lithium-ion battery (LIB) electrode materials with much higher energy densities, materials that operate via conversion (rather than topotactic (or insertion)) reactions have received considerable attention. These conversion materials can accommodate multiple electron transfers per redox centre via the equation $M_aX_b + (b \cdot n)Li^+ + (b \cdot n)e^- = aM + bLi_nX$ (X = F, O, S, etc)[1], leading to large specific capacities. Because fluorine's high-electronegativity imparts a higher average voltage for reaction involving transition metal (TM) fluorides (MF_x) than those of their oxide or sulfide counterparts[1], they can be used as LIBs cathode materials[2]. Recent developments of fluoride-ion-based solid-state batteries[3-7] and liquid fluoride[8] ion-conducting electrolytes has prompted further renewed interest.

Among all the MF_x phases, FeF_3 has received the most attention[1] due to its low cost and toxicity[9] and high energy density (1951 Wh/kg, cf. 1519 and 1874 Wh/kg for FeF_2 and CuF_2, respectively)[2]. Unlike FeF_2/CuF_2, FeF_3 exhibits an additional high voltage plateau generally assigned to an insertion (or intercalation) process[10,11] (Fig. 1a-b). This process alone shows a (practical) capacity of ≈ 200 mAh/g (cf. ≈ 170 mAh/g for both $LiCoO_2$ and $LiFePO_4$) and is largely reversible[12] with a smaller overpotential than its subsequent (nominal) conversion process[13] making FeF_3 a promising insertion cathode. Because of its intrinsically poor electronic conductivity[2] FeF_3 must be nanostructured (and embedded in a conductive matrix)[10,14] to enable good electrochemical performance. This nanosizing and the lack of long-range order on lithiation renders structure solution via X-ray diffraction (XRD) challenging[13]. While local probes, including solid-state nuclear magnetic resonance (NMR)[10] spectroscopy, X-ray absorption spectroscopy (XAS)[11,15] and pair distribution function (PDF)[10] analyses, have been used, no clear consensus has emerged[11,15], indicating structural complexity. Numerous studies[10,11,13,14,16-19] have correlated FeF_3's phase behaviour in the insertion regime with reaction kinetics, but different mechanisms have been proposed, largely due to conflicting reports of the structure of the lithiated $Li_xFe_yF_3$ phases. The majority of studies agree that the rhombohedrally-distorted ReO_3-structure ($R\bar{3}c$) comprising corner sharing FeF_6 groups (Fig. 1c) transforms into an edge-sharing trirutile Li_xFeF_3 phase ($P4_2/mnm$), albeit with different x values[10,15,17], a transformation that involves considerable change in anion-packing and Fe-ordering. Less radical structural changes from $R\bar{3}c$ to $R3c$[11] or to a slightly-distorted rhombohedral phase[13] have also been proposed.

To circumvent the analytical challenges, we compare the results obtained from both micro- (ca 0.2 um) and nano-meter (ca 7 nm) FeF_3 (denoted as m- and n-FeF_3, respectively), which contain similar features in their electrochemistry (Fig. 1a and S1). A charge-flipping method was applied against the electron diffraction (ED) data to solve the structures of the intermediate phases that forms on lithiating m-FeF_3. With this new structural insight we revisited FeF_2 and CuF_2 and solved the structure of the nanosized intermediate by applying our newly developed approach based on non-negative matrix factorisation (NMF) algorithm[20] to PDF data, recently developed to study solid mixtures[20], and which does not require any prior knowledge of the number and nature of the phases. Our results show that the general lithiation pathways in FeF_3 (hexagonal close packed/*hcp*) and FeF_2 (tetragonal close packed[21]/*tcp*) are dominated by topotactic diffusion-controlled *displacement* mechanisms. This new mechanistic insight provides a rationale for the path hysteresis[22] seen in these materials.

Lithiated m-FeF_3 structural determination

Given the role of the initial lithiation processes in FeF_3 in steering the subsequent reactions, we start by identifying the phases generated on lithiation of m-FeF_3. The *ex situ* XRD patterns of all cycled samples (Fig. 2a and S2) contain a new broad feature comprising two distinct components at 26.6° and 28.0°, 2θ, whose relative intensities vary with state-of-charge. Other noticeable changes include i) a large intensity reduction for the (012) reflection ascribed to Fe migration to the neighbouring sites[19] and ii) the emergence of low-angle (003) and $(01\bar{1})$ reflections (indexed based on the same hexagonal lattice) indicating the loss of *c*-glide planes. Additional new reflections are seen at the states corresponding to nominal formulae $Li_{0.15}FeF_3$ and $Li_{0.5}FeF_3$, denoted as "Li 0.15" and "Li 0.5", respectively (Fig. 2b), suggesting a two-step insertion process involving the sequential formation of new phases (denoted as *A*- and *B*-$Li_xFe_yF_3$). These reflections are close to those of pristine m-FeF_3, underlying the structural correlations between FeF_3 and $Li_xFe_yF_3$.

An assessment of the hetto- and aristo-types of (*i.e.*, the low and high symmetry structures arising from) the ABX_3 ($R\bar{3}c$) structure[23] was made (Fig. S3) and a rhombohedral $R3$ cell was chosen as the starting model for refinement. The refined structures for both *A*- and *B*-$Li_xFe_yF_3$ contain a near-perfect *hcp* F^- lattice, with the six different crystallographic Fe sites $a_1 - a_6$ (Fig. 1c) generated from symmetry reduction showing distinct Fe occupancies consistent with $R3$ and $R3c$ symmetry for the *A*- and *B*-phases, respectively (see Sec. S1 for details); note the higher symmetry for the *B*-phase indicates an increased ordering of the Fe atoms. Based on the new symmetry, iterative refinements (Fig. S4-5) were performed and the derived structures were verified via PDF analysis (Fig. 2c-d and S6). Surprisingly, the inclusion of a considerable amount of non-crystalline rutile FeF_2 (~1.5 nm) was required to achieve a good fit to the short-range PDF pattern of all cycled samples. The inclusion of FeF_2 also accounts for the broad XRD feature at 26.6° 2θ (Fig. S2), however, the 28.0° 2θ scattering feature remains unmodelled, indicating that some structure/phase information is still absent in our model.

ED measurements were then performed on samples "Li 0.25" and "Li 0.6", whose Li compositions are associated with the highest concentrations of the *A*- and *B*-phases, respectively, allowing each phase to be studied individually. The ED data of *A*-$Li_xFe_yF_3$ show different systematic absences than those generated in simulations using pristine FeF_3 (*R*-3c) (Fig. 3b and e) and the XRD-derived *A*-phase structure (*R*3) (Fig. 3c and f), with i) the emergence of {100}-type reflections as the shortest *g*-vectors (Fig. 3a) and ii) the observation of all (00*l*) reflections (Fig. 3d). These observations indicate that a further symmetry lowering all the way from FeF_3's symmetry (*R*-3c) to a primitive lattice (e.g., *P*3) is required to describe this phase. Furthermore, the positions with the highest intensities in the first and second row of the ED reflections parallel to the *c** (Fig. 3d) correspond to the (013) and (023) reflections rather than (012) and (024) in FeF_3, providing compelling evidence for a significant change in Fe positions. The charge-flipping algorithm[24] (Sec. S2) was then applied using the intensities extracted from the ED pattern of an *A*-$Li_xFe_yF_3$ crystal to determine the projected structure of the *A*-phase. The resulting model features "zig-zag"-arranged Fe sites (Fig. 3g). Scanning electron diffraction (SED)[25], performed to evaluate the spatial distribution of the *A*-phase (Sec. S3), revealed a two-phase coexistence in one particle (Fig. 3i) with the *A*-phase (Fig. 3j) surrounding the pristine FeF_3 phase (Fig. 3k), suggesting $Li_xFe_yF_3$ grows coherently from the parent phase. In addition, a less crystalline phase was also detected (Fig. 3l) which can be indexed to rutile FeF_2 (Fig. 3d). The ED data of *B*-$Li_xFe_yF_3$ (Fig. S7) matches the *R*3c model obtained from XRD with some weak additional reflections also present suggesting minor distortions, *i.e.*, local symmetry reduction (Sec. S4).

Structure and energetics of *A*-$Li_xFe_yF_3$

Density functional theory (DFT) calculations (Sec. S5) performed to evaluate any possible charge ordering in the zig-zag *A*-$Li_xFe_yF_3$ structure described above, and to rationalise the weak ferromagnetism observed for this phase (Sec. S6 and Fig. S8), returned a *P*312 model (Table S1) with alternating Fe^{3+} and Fe^{2+} ions separated by *c*/3 along the *c*-axis. This structure has Li in the Fe^{3+} layers (Fig. 3h) with a Fe ordering that gives rise to the strong (013) reflections seen experimentally (Fig. S9). Importantly, the overall energy of this structure is only 0.03 eV per formula unit less stable than the thermodynamic minimum, trirutile-$Li_{0.5}FeF_3$ (Table S2). However, despite the consistency in TM ordering between the ED- and DFT-derived models, there are a few reflections/peaks (e.g., the (013)) that are either notably broadened in the experimental XRD pattern or not seen in the simulated XRD/PDF data (Fig. S10-11). This is ascribed to the different sample illumination sizes of the electron and X-ray scattering experiments, the larger area probed by the latter rendering the XRD/PDF-derived model an average representation of the *A*-phase. In contrast, the smaller illuminated area in ED probes the local-medium range structure, which is not necessarily affected by additional (macroscopic) structure defects.

To explain the origin of the broadening of the (013) reflection in the experimental XRD pattern, a structure incorporating stacking disorder of the *P*312 cell (referred to as the faulted-*P*312 model) was implemented (Fig. 4a). In addition to the improved agreement in the XRD pattern (Fig. 4d), this faulted model can also rationalise the emergence of the (01*l*) and (02*l*) reflections in the ED patterns (Fig. S12). However, the fit to the PDF data (which represents the average local atomic structure) is still poor (see

arrows in Fig. 4e and S11). A re-evaluation of cation ordering in the faulted-*P*312 model surprisingly showed that it could be constructed by using a simpler and smaller building block (Fig. 4a), with charge ordering between multivalent cations equivalent to that found in α-$LiMn^{2+}Fe^{3+}F_6$ (Fig. 4b), differing only in (some of the) Li positions (i.e., 1/3 of Li is located in the TM^{2+} layer in α-$LiMn^{2+}Fe^{3+}F_6$). α-$LiMn^{2+}Fe^{3+}F_6$ reversibly transforms to the high-temperature β-$LiMn^{2+}Fe^{3+}F_6$ phase (both *P*321) above approximately 500 °C, indicating their similar energies[26]. The β-structure is related to the α-form by an inversion of the Li^+ and Fe^{3+} positions. Inspired by the $LiMnFeF_6$ dimorphism[26], we built a new faulted *A*-$Li_xFe_yF_3$ model (Fig. 4c) incorporating disordered stacking of α- and β-$LiFe^{2+}Fe^{3+}F_6$ building blocks (in a ratio of 50:50) with cation orderings (including Li) mirroring those of α/β-$LiMn^{2+}Fe^{3+}F_6$. The displacement vectors for the α- and β-segments were defined so as to minimise face-shared Fe. Given that the α/β ratio and fault probabilities are both variables, the agreement between the experiments and derived XRD and PDF simulations (Fig. 4d-e) is good. The majority of Li (5/6) resides in the Fe^{3+} layer in the new faulted model, still in good agreement with the DFT prediction.

Insertion- and full-cycle mechanisms of n-FeF_3

A careful comparison of the XRD and PDF data of n-FeF_3 and m-FeF_3 obtained during cycling shows considerable structural similarity between the phases generated in the two systems on lithiation (Fig. 5a-c and S13). PDF analysis confirmed the presence of *A*-/*B*-$Li_xFe_yF_3$ and nano-FeF_2 upon lithiation of n-FeF_3 (Fig. 5b-c). However, unlike the two-phase pathway identified in m-FeF_3 for the *A*-*B* phase transition, a solid-solution process from A-B was seen for n-FeF_3.

We now introduce the newly identified lithiated phases into the Li-Fe-F phase diagram[27], using the diagram to navigate through the intricate lithiation processes (Fig. 5d). During the initial lithiation, FeF_3 undergoes a three-phase reaction (I) giving rise to *A*-$Li_xFe_{1-\delta}F_3$ and FeF_2:

$$x\ \mathrm{Li} + (1+2\delta)\ \mathrm{FeF_3} \rightarrow A\text{-}\mathrm{Li}_x\mathrm{Fe}_{1-\delta}\mathrm{F_3} + 3\delta\ \mathrm{FeF_2} \qquad \text{I : insertion + displacement}$$

The preservation of the *hcp* anion framework between FeF_3 and *A*-$Li_xFe_{1-\delta}F_3$ complies with a *displacement*-like mechanism[28] with the extruded FeF_2 with its *tcp* lattice being the displaced species. One potential endpoint of this reaction is the charge-ordered phase *A*-$LiFe^{2+}Fe^{3+}F_6$ ($x = 0.5$ and $\delta = 0$), a phase that is formed if the reaction involves insertion only. However, the *A*-phase seen electrochemically must contain Fe-deficiency ($\delta > 0$), since FeF_2 formation is also observed. Note that the idealised *A*-$LiFe^{2+}Fe^{3+}F_6$ has the same composition as trirutile – the structure proposed previously[10,15,17], but the *A*-phase has an *hcp* rather than a *tcp* lattice.

Li insertion into and migration in FeF_3, and the concurrent reduction of Fe^{3+} to Fe^{2+}, will be relatively rapid; this, in combination with charge ordering between Fe^{2+} and Fe^{3+}, will trigger the *R*-3c – *R*3 rearrangement of the F sublattice and the nucleation and growth of the new phase (*A*) . Since the rearrangement of the F sublattice is only minor it will likely be associated with only a small activation barrier. In contrast, migration of the highly charged $Fe^{2+/3+}$ ions and the significant rearrangement of the F sublattice both required to form FeF_2 will be associated with a much higher activation barrier, and this competing reaction will be sluggish. The driving force for this reaction reflects the thermodynamic stability of the rutile sublattice[21] with respect to the *hcp* sublattice as Fe is reduced. (N.b., DFT indicates that *A*-$LiFe^{2+}Fe^{3+}F_6$ is metastable with respect to *trirutile* $LiFe^{2+}Fe^{3+}F_6$). We tentatively suggest that more FeF_2 was formed in the m-FeF_3 sample, in part because this reaction was performed at a higher temperature, but the effect of particle size on the *A*-$LiFe^{2+}Fe^{3+}F_6/FeF_2$ interfacial energy may also play a role. The formation of the electronically insulating layer of nano-FeF_2 on the surface of *A*-$Li_xFe_{1-\delta}F_3$ results in a passivation layer, reducing contact with carbon matrix and increasing interfacial ionic resistance. This, combined with the albeit small (relative to that of FeF_2 formation) activation barrier to form *A*-$Li_xFe_{1-\delta}F_3$ helps rationalise the temperature-dependent cycling behaviour where elevated temperatures ($\geq$ 60℃) were found critical – particularly for the micron phase – to reduce the overpotential in the insertion regime;[19,29] these observation helps to reconcile an inconsistency in the literature – namely the observation of large overpotential for a process that is often described as a simple intercalation reaction.[19,29]

Upon further discharge, process II follows the tie line from *A*-$Li_xFe_{1-\delta}F_3$ to *B*-$Li_{1+2\delta}Fe_{1-\delta}F_3$ via an intercalation-type reaction with Fe being completely reduced to Fe^{2+} in *B*, a process that also involves Fe cation migration to form a Fe sublattice that complies with the higher symmetry (*R*3*c*):

$$(1+ 2\delta - x)\ \mathrm{Li} + A\text{-}Li_xFe_{1-\delta}F_3 \xrightarrow[\text{two phase (m}-FeF_3)]{\text{solid solution (n}-FeF_3)} B\text{-}Li_{1+2\delta}Fe^{2+}{}_{1-\delta}F_3 \quad \text{II : intercalation + cation migration}$$

Whilst the lithiation in m-FeF_3 is two phase, n-FeF_3 undergoes a single-phase mechanism, consistent with the gradual shift in the ^{6}Li NMR resonance of this phase towards lower ppm observed in our previous ^{6}Li NMR study of n-FeF_3 (Extended Data Fig. 1).[10] This size effect has analogies with the mechanisms seen for $LiFePO_4$: a two phase reaction involves the formation and movement of a (high energy) interface between the two phases, which will have a higher surface area relative to the volume of the particle as particle size decreases, and thus a higher energy.[30] This phenomenon can help favour a solid solution mechanism in smaller particles. The smaller polarisation in n-FeF_3 enables a higher completion rate of this phase transition at higher voltages (Fig. 1a), however, full capacity can be achieved at 60 °C on opening up the voltage window to ≈ 1.5 V (Fig. S1).

Upon completion of reaction II, a sudden voltage drop is observed signifying the end of the "insertion" discharge reaction. Subsequent charging at this point results in reactions II' and I' (the reverse of processes II and I) to reform the *A*-phase and FeF_3, respectively. However, there is only a partial reformation of FeF_3 (Fig. 5e) – more pronounced in micron size particles − presumably due to poor contact between FeF_2 and the *A*/*B*-phases; this can be effectively mitigated by employing nanostructured materials and/or elevated operating temperatures, decreasing the distances over which Fe atoms have to migrate, and enhancing transport, respectively[29].

In the "conversion" regime, further discharge of the *B*-phase and FeF_2 proceed via separate routes. The lithiation of *B*-$Li_{1+2\delta}Fe_{1-\delta}F_3$ first (step III) involves the formation of another intermediate *C*-$Li_{1+2\eta}Fe^{2+}{}_{1-\eta}F_3$, whose structure (Sec. S7) is closely related to the *B*-phase, involving another topotactic *displacement* process (III). Further lithiation of the *C*-phase finally triggers the reconstruction of the F^- sublattice from *hcp* to *fcc* in LiF forming a Fe (~ 2 nm) and LiF (> 3 nm) composite:

$$2(\eta - \delta)\ \mathrm{Li} + B\text{-}Li_{1+2\delta}Fe^{2+}{}_{1-\delta}F_3 \rightarrow C\text{-}Li_{1+2\eta}Fe^{2+}{}_{1-\eta}F_3 + (\eta - \delta)\ \mathrm{Fe} \qquad \text{III : displacement}$$

$$2(1 - \eta)\ \mathrm{Li} + C\text{-}Li_{1+2\eta}Fe_{1-\eta}F_3 \rightarrow 3\ \mathrm{LiF} + (1 - \eta)\ \mathrm{Fe} \qquad \text{IV : conversion}$$

Subsequent charge follows reversible pathways from process IV' all the way to process I' (Fig. 5d and S14). More information concerning the charge process (Sec. S8) and the second cycle (Fig. S15) is given in the SI.

Mechanistic revisit of rutile fluorides

Both the importance of FeF_2 as a cathode material[31-33] and our identification of two metastable $Li_{1+2x}Fe_{1-x}F_3$ phases situated on the LiF-FeF_2 tie line (Extended Data Fig. 2), prompted a reanalysis of our original FeF_2 PDF data (Fig. S16) using a novel analytical method based on Metropolis NMF algorithm[20]. Our analysis (Video S1) of the first discharge cycle uncovered (at least) one additional phase in the data (Fig. 6a and S17) whose presence is supported by a weak Bragg feature at around 20° 2θ (Fig. S16b). While a unique solution is difficult given the small size of this phase (~ 1.5 nm), its atomic ordering could be well modelled using an orthorhombic Li_2FeF_4 (*Cmmm*)[34] phase whose (020) reflection coincides with the observed weak scattering feature. Notably, this structure exhibits an evident group-subgroup relationship[23] with the reactant ($P4_2/mnm$) and the LiF product ($Fm\bar{3}m$) (Fig. 6b). Inclusion of this Li_2FeF_4 phase in our refinements leads to a significantly improved fit (Fig. S18c) with the refined crystallite size almost constant (~ 1.5 nm) during the whole cycle. In addition, Li_2FeF_4 is also identified in FeF_2's charge process (Fig. S18b) and at the end of the discharge/early in the charge of FeF_3 (Fig. S18e-f) – likely via a reaction involving extruded FeF_2. The results imply that the intermediate Li_2FeF_4 is present – at least in part – as an interface, whose formation is likely to mitigate the substantial

structural difference between the reactant FeF_2 and product LiF. To help validate this hypothesis, we constructed an interface model ($LiF|Li_2FeF_4|FeF_2$) in which Li_2FeF_4 is coherently connected to LiF and FeF_2 units according to their underlying symmetry relationships (Fig. 6c). Based our DFT studies of this interface model, as well as an evaluation of the energies of the related phases under lattice matching conditions (Fig. S19), we conclude that the inclusion of the Li_2FeF_4 interfacial component is energetically favoured (Sec. S9). Therefore, although FeF_2 has been widely perceived to function via *conversion* mechanism, our analyses point to a reversible two-step topotactic *displacement* pathway (V_I and V_{II}). We have further verified that a similar mechanism occurs in CuF_2 (Sec. 10 and Video S2) and have identified an orthorhombic Li_2CuF_4 (*Cmca*)[34] phase as the intermediate phase, with a different Li/Cu ordering scheme (Fig. S20-22 for full details). The idealised and simplified reactions can, therefore, be written as:

$$2x\ \mathrm{Li} + \mathrm{MF_2} \rightarrow \mathrm{Li_{2x}M_{1-x}F_2} + x\ \mathrm{M} \qquad (\mathrm{M = Fe, Cu};\ 0 < x \leq 0.5)\ \ V_I: \text{displacement}$$

$$2\ \mathrm{Li} + \mathrm{Li_2MF_4} \rightarrow 4\ \mathrm{LiF} + \mathrm{M} \qquad (\mathrm{M = Fe, Cu}) \qquad V_{II}: \text{displacement}$$

We note that earlier TEM studies also reported a topotactic lithiation of FeF_2[31], but despite sustained efforts[31-33,35,36], and with the exception of our earlier ^{6}Li NMR study[10], the presence of an intermediate was not confirmed in other studies of the bulk phases. The results presented here differ from those in a recent TEM study[32] which reported the formation of an Fe^{3+}-containing trirutile intermediate phase ($LiFe^{2+}Fe^{3+}F_6$) upon lithiation of FeF_2. We note that the high sensitivity of FeF_x to electron radiation damage[37] at high dose rates[32] (explored further in the Sec. S11) highlights the need to ensure that the structural models proposed with TEM data are consistent with the results acquired from multiple structural techniques (Fig. S23-24). Given the structure flexibility of these orthorhombic structures in accommodating symmetry changes and lattice-/atomic distortions during the *tcp* (rutile)-*fcc* (rocksalt) transition, we infer that a number of other rutile-related TM fluorides may follow a similar *displacement* process. Further experimental and computation studies are needed to understand the role that these buffer phases play in controlling reactivity and rates.

Towards a comprehensive account of FeF_3-FeF_2 system

Based on the improved mechanistic knowledge of rutile's phase behaviour upon cycling, we now consider the relationship between FeF_3 and FeF_2 given their coexistence during the whole FeF_3 cycle. It is worth noting that while some studies also observed FeF_2[15,29] upon lithiation of FeF_3, the formation of this rutile phase derived from a phase transition of the whole FeF_3 particle. However, we stress that the original *hcp* F^- lattice is largely retained all the way to the last lithiation step to form *fcc* LiF. The F^- lattice transition from *hcp* (FeF_3) to *tcp* (rutile) only occurs at the surface of the FeF_3 particle. Furthermore, in contrast to the occurrence of an intermediate stage in FeF_2's lithiation to form LiF (+ Fe) via a *tcp-fcc* lattice transition (reaction V_I and V_{II}), the *hcp-fcc* transformation in the lithiation of *C*-$Li_{1+2\eta}Fe_{1-\eta}F_3$ (reaction IV) proceeds via a reconstructive *conversion* reaction. A *fcc-hcp* reconversion takes place concurrently with the *fcc-tcp* transition during the charge of FeF_3, while only the latter was observed in FeF_2 (within the same voltage window). Significantly more FeF_2 relative to $Li_xFe_yF_3$ is formed upon charge of the FeF_3 system, suggesting that the topotactic *fcc-tcp* transition is the favoured delithiation process. This work suggests that the nature of the interfaces may play a role in controlling the amount of FeF_3 (cf. FeF_2) upon charge, an important factor which likely needs to be considered in the preparation of FeF_3/FeF_2 electrodes using pre-lithiated LiF/Fe mixtures[38-40].

As a final point, we highlight that the lithiation and delithiation steps for both FeF_3 and MF_2 are primarily diffusion-controlled processes dominated by *displacement* mechanisms, whose kinetic behaviour mainly depends on the mobility difference between the displaced species.[22] During discharge, the concurrent Li insertion and M extrusion is limited by the TM diffusion due to the generally faster Li transport, resulting in almost invariant overpotentials, hence flat operating voltages; while upon charge, a more rapid Li removal than M insertion leads to gradually increased overpotentials as Li is extracted, resulting in more sloping voltage profiles. This phenomenon has been described as "path hysteresis" and is characteristic for displacement reactions.[22] Hence, while structure engineering

remains important to improve the rate performance, we note that effective mitigation of intrinsic path hysteresis will require exploitation of material systems with improved metal (ion) mobilities.

To summarise, we have performed a comprehensive investigation of FeF_3's structural behaviour as a cathode material for LIBs and revisited our previous work on FeF_2 and CuF_2[41]. We demonstrated the need to obtain crystallographic information over a wide range of length scales to develop a compelling atomistic model that could be tested against all the data. Our study revealed an unexpectedly complicated lithiation process during FeF_3's initial discharge, involving displacement of nanoscale FeF_2 and concurrent formation of *A*-$Li_xFe_yF_3$, whose intricate structure contains faulted stacking of motifs that are isostructural to *α*- and *β*-$LiMnFeF_6$. Further lithiation of the *A*-phase and FeF_2 proceed via distinct routes that are dominated by displacement reactions based on topological relationships between these fluorides' F^- lattices (*hcp*/*tcp*) and that in the rocksalt product (*fcc*). This renewed mechanistic insight reveals an underlying principle that may serve as a reference model for a wider range of isomorphic binary fluorides and ternary systems[36,42]; it also rationalises the intrinsic path hysteresis, suggesting that it could be mitigated by employing displaced species with enhanced mobilities. From a methodological perspective, this work demonstrates the viability of our novel analytical approach combining PDF and NMF to uncover minor species within a heterogenous system, with broader implications beyond energy storage.

REFERENCES

1 Cabana, J., Monconduit, L., Larcher, D. & Palacín, M. R. Beyond Intercalation-Based Li-Ion Batteries: The State of the Art and Challenges of Electrode Materials Reacting Through Conversion Reactions. *Adv. Mater.* **22**, E170-E192 (2010).

2 Amatucci, G. G. & Pereira, N. Fluoride based electrode materials for advanced energy storage devices. *J. Fluorine Chem.* **128**, 243-262 (2007).

3 Grenier, A. *et al.* Solid Fluoride Electrolytes and Their Composite with Carbon: Issues and Challenges for Rechargeable Solid State Fluoride-Ion Batteries. *J. Phys. Chem. C* **121**, 24962-24970 (2017).

4 Thieu, D. T. *et al.* CuF_2 as Reversible Cathode for Fluoride Ion Batteries. *Adv. Funct. Mater.* **27**, 1701051 (2017).

5 Zhang, L., Anji Reddy, M. & Fichtner, M. Development of tysonite-type fluoride conducting thin film electrolytes for fluoride ion batteries. *Solid State Ion.* **272**, 39-44 (2015).

6 Anji Reddy, M. & Fichtner, M. Batteries based on fluoride shuttle. *J. Mater. Chem.* **21**, 17059-17062 (2011).

7 Gschwind, F. *et al.* Fluoride ion batteries: Theoretical performance, safety, toxicity, and a combinatorial screening of new electrodes. *J. Fluorine Chem.* **182**, 76-90 (2016).

8 Davis, V. K. *et al.* Room-temperature cycling of metal fluoride electrodes: Liquid electrolytes for high-energy fluoride ion cells. *Science* **362**, 1144 (2018).

9 Reddy, M. A. & Fichtner, M. in *Advanced Fluoride-Based Materials for Energy Conversion* (ed Henri Groult) 51-76 (Elsevier, 2015).

10 Yamakawa, N., Jiang, M., Key, B. & Grey, C. P. Identifying the Local Structures Formed during Lithiation of the Conversion Material, Iron Fluoride, in a Li Ion Battery: A Solid-State NMR, X-ray Diffraction, and Pair Distribution Function Analysis Study. *J. Am. Chem. Soc.* **131**, 10525-10536 (2009).

11 Zhang, W. *et al.* In Situ Electrochemical XAFS Studies on an Iron Fluoride High-Capacity Cathode Material for Rechargeable Lithium Batteries. *J. Phys. Chem. C* **117**, 11498-11505 (2013).

12 Kim, S.-W., Seo, D.-H., Gwon, H., Kim, J. & Kang, K. Fabrication of FeF_3 Nanoflowers on CNT Branches and Their Application to High Power Lithium Rechargeable Batteries. *Adv. Mater.* **22**, 5260-5264 (2010).

13 Tan, H. J. *et al.* Electrochemical Cycling and Lithium Insertion in Nanostructured FeF_3 Cathodes. *J. Electrochem. Soc.* **161**, A445-A449 (2014).

14 Badway, F., Cosandey, F., Pereira, N. & Amatucci, G. G. Carbon Metal Fluoride Nanocomposites. *J. Electrochem. Soc.* **150**, A1318 (2003).
15 Li, L. *et al.* Origins of Large Voltage Hysteresis in High-Energy-Density Metal Fluoride Lithium-Ion Battery Conversion Electrodes. *J. Am. Chem. Soc.* **138**, 2838–2848 (2016).
16 Liu, P., Vajo, J. J., Wang, J. S., Li, W. & Liu, J. Thermodynamics and Kinetics of the Li/FeF_3 Reaction by Electrochemical Analysis. *J. Phys. Chem. C* **116**, 6467-6473 (2012).
17 Li, L. *et al.* Visualization of electrochemically driven solid-state phase transformations using operando hard X-ray spectro-imaging. *Nat. Commun.* **6**, 6883 (2015).
18 Zhou, M., Zhao, L., Kitajou, A., Okada, S. & Yamaki, J.-i. Mechanism on exothermic heat of FeF_3 cathode in Li-ion batteries. *J. Power Sources* **203**, 103-108 (2012).
19 Badway, F., Pereira, N., Cosandey, F. & Amatucci, G. G. Carbon-Metal Fluoride Nanocomposites: Structure and Electrochemistry of FeF_3 : C. *J. Electrochem. Soc.* **150**, A1209-A1218 (2003).
20 Geddes, H. S., Blade, H., McCabe, J. F., Hughes, L. P. & Goodwin, A. L. Structural characterisation of amorphous solid dispersions via metropolis matrix factorisation of pair distribution function data. *Chem. Commun.* **55**, 13346-13349 (2019).
21 West, A. R. & Bruce, P. G. Tetragonal-packed crystal structures. *Acta Crystallogr. B* **38**, 1891-1896 (1982).
22 Yu, H. C. *et al.* Designing the next generation high capacity battery electrodes. *Energy Environ. Sci.* **7**, 1760-1768 (2014).
23 Müller, U. *Symmetry relationships between crystal structures: applications of crystallographic group theory in crystal chemistry*. Vol. 18 (OUP Oxford, 2013).
24 Oszlanyi, G. & Suto, A. Ab initio structure solution by charge flipping. *Acta Crystallogr. A* **60**, 134-141 (2004).
25 Rauch, E. *et al.* Automatic crystal orientation and phase mapping in TEM by precession diffraction. *Microscopy and Analysis* **22**, S5-S8 (EU) (2008).
26 Courbion, G., Jacoboni, C. & De Pape, R. The dimorphism of $LiMnFeF_6$: A new kind of cationic order in the structural type Na_2SiF_6. *J. Solid State Chem.* **45**, 127-134 (1982).
27 Doe, R. E., Persson, K. A., Meng, Y. S. & Ceder, G. First-Principles Investigation of the Li−Fe−F Phase Diagram and Equilibrium and Nonequilibrium Conversion Reactions of Iron Fluorides with Lithium. *Chem. Mater.* **20**, 5274-5283 (2008).
28 Goodenough, J. B. & Park, K.-S. The Li-Ion Rechargeable Battery: A Perspective. *J. Am. Chem. Soc.* **135**, 1167-1176 (2013).
29 Tawa, S., Matsumoto, K. & Hagiwara, R. Reaction Pathways of Iron Trifluoride Investigated by Operation at 363 K Using an Ionic Liquid Electrolyte. *J. Electrochem. Soc.* **166**, A2105-A2110 (2019).
30 Van der Ven, A., Garikipati, K., Kim, S. & Wagemaker, M. The Role of Coherency Strains on Phase Stability in Li_xFePO_4: Needle Crystallites Minimize Coherency Strain and Overpotential. *J. Electrochem. Soc.* **156**, A949 (2009).
31 Karki, K. *et al.* Revisiting Conversion Reaction Mechanisms in Lithium Batteries: Lithiation-Driven Topotactic Transformation in FeF_2. *J. Am. Chem. Soc.* **140**, 17915-17922 (2018).
32 Xiao, A. W. *et al.* Understanding the conversion mechanism and performance of monodisperse FeF_2 nanocrystal cathodes. *Nat. Mater.* **19**, 644-654 (2020).
33 Wang, F. *et al.* Conversion Reaction Mechanisms in Lithium Ion Batteries: Study of the Binary Metal Fluoride Electrodes. *J. Am. Chem. Soc.* **133**, 18828-18836 (2011).
34 Jain, A. *et al.* Commentary: The Materials Project: A materials genome approach to accelerating materials innovation. *APL Materials* **1**, 011002 (2013).
35 Wang, F. *et al.* Tracking lithium transport and electrochemical reactions in nanoparticles. *Nat. Commun.* **3**, 1201 (2012).
36 Wang, F. *et al.* Ternary metal fluorides as high-energy cathodes with low cycling hysteresis. *Nat. Commun.* **6**, 6668 (2015).
37 Cosandey, F., Al-Sharab, J. F., Badway, F., Amatucci, G. G. & Stadelmann, P. EELS Spectroscopy of Iron Fluorides and FeF_x/C Nanocomposite Electrodes Used in Li-Ion Batteries. *Microsc. Microanal.* **13**, 87-95 (2007).

38 Sun, Y. *et al.* In Situ Chemical Synthesis of Lithium Fluoride/Metal Nanocomposite for High Capacity Prelithiation of Cathodes. *Nano Lett.* **16**, 1497-1501 (2016).
39 Hori, H. & Okada, S. Reconversion Reaction of LiF/Fe Composite Thin Film Cathodes for Lithium-Ion Battery. *Electrochemistry* **83**, 909-913 (2015).
40 Li, T., Chen, Z. X., Ai, X. P., Cao, Y. L. & Yang, H. X. LiF/Fe nanocomposite as a lithium-rich and high capacity conversion cathode material for Li-ion batteries. *J. Power Sources* **217**, 54-58 (2012).
41 Hua, X. *et al.* Comprehensive Study of the CuF_2 Conversion Reaction Mechanism in a Lithium Ion Battery. *J. Phys. Chem. C* **118**, 15169-15184 (2014).
42 Huang, Q. *et al.* Fading Mechanisms and Voltage Hysteresis in FeF_2–NiF_2 Solid Solution Cathodes for Lithium and Lithium-Ion Batteries. *Small* **15**, 1804670 (2019).

METHODS

Materials preparation. m-FeF_3 electrode mixtures were prepared by mixing 75 *wt%* FeF_3 (sigma-aldrich) and 25 *wt%* carbon manually ground in an agate mortar. n-FeF_3, FeF_2, and CuF_2 nanocomposites were prepared as described elsewhere[41,43]. Their electrode mixtures were prepared by mixing 90 *wt*% of the nanocomposite with an additional 10 *wt*% of carbon that were manually ground in an Agathe mortar. The resulting loose powders were directly used as cathodes without any additional binder. Swagelok cells were assembled with 3-5 mg of cathode powders, a Whatman glass fibre separator wetted with electrolyte and a Li metal disk. The electrolyte was 1M $LiPF_6$ in 1:1(v/v) EC/DMC. Electrochemical tests were carried out using a Bio-Logic potentiostat. Samples for HRXRD, PDF, ED, and SQUID were recovered from batteries stopped at the selected states of charge, disassembled inside the glovebox and rinsed with DMC twice before drying and filling the capillaries or SQUID capsule. All the charged samples (apart from the ones at the early charge) were prepared at selected voltages because using voltage criterion to choose critical state of charge is a more reliable experimental control at late charge. A drop of the DMC suspension was used for TEM grid preparation. TEM grids were sealed under Argon until transferred into the TEM.

X-ray diffraction and total scattering. Ex situ HRXRD experiments were performed at the Advanced Photon Source (APS) beamline 11-BM (λ = 0.4136 Å) using a 12-channel analyzer detector array. Ex situ X-ray total scattering were performed at APS beamline 11-ID-B (λ = 0.2127 Å) and Diamond beamline I15-1 (λ = 0.1617 Å) both using an area detector. PDF patterns (Q_{max} = 24 $Å^{-1}$) were generated using Fit2D[44]/DAWN[45] and PDFgetX2[46] for data reduction and normalisation, respectively. All samples were sealed in either Kapton or quartz capillaries. XRD and PDF analyses were performed using TOPAS v4 / GSAS-II[47] and PDFgui[48] / DISCUS[49] programs respectively. Stacking faults was modelled using DIFFaX[50]. In situ X-ray total scattering data collection for CuF_2 is described elsewhere[41].

Electron diffraction. Electron diffraction experiments were performed on a Philips CM30 TEM operating at 300kV. A Nanomegas Spinningstar apparatus was used to produce a beam precession angle of 1°. Images were recorded on Ditabis imaging plates and processed using software developed in the Electron Microscopy Group in Cambridge. Scanning electron diffraction experiments were performed on a Philips CM300 FEGTEM operating at 300kV equipped with a Nanomegas Digistar apparatus to generate a scan area of 275nm x 275nm with a scan step of 2.5nm. Diffraction patterns were recorded on a high speed external digital camera and phase and orientation analysis was performed using the ASTAR software package.

SQUID. Magnetization was measured on a Quantum Design Magnetic Properties Measurement System (MPMS) with a superconducting quantum interference device (SQUID) magnetometer. Zero Field cooled (ZFC) Field cooled (FC) (100 Oe) magnetic susceptibility χ(T) was measured in the temperature range 2-300K. Magnetization vs Magnetic field (H) measurements were recorded in the 0-5 Tesla range at 200K on pristine FeF_3 and dis Li 0.4.

Density functional theory calculation. Combined crystal and magnetic structure predictions were performed using Ab Initio Random Structure Searching (AIRSS)[51,52]. Energy optimisations were performed using CASTEP[10]. In order to remain consistent with the composition of the trirutile phase ($P4_2/mnm$)[10], calculations were performed for a stoichiometry of $Li_{0.5}FeF_3$ and the cell parameters were adopted from the HRXRD refinement. The calculation was performed using a 700 eV plane-wave cut-off energy and a 5×5×2 Monkhorst-Pack *k*-point grid using the PBE functional. GGA+U was used with a U on the iron *d*-channel of 4 eV. Full computational details are available as part of the supplied computed data. The energy calculation for the interface model was performed using the same setting.

Non-negative matrix factorisation. The NMF approach followed closely the Metropolis Matrix Factorisation (MMF) method reported earlier[20], which uses the MMC algorithm to carry out NMF[53]. The NMF analysis was performed on renormalised PDFs to satisfy the non-negative criterion of NMF.

The renormalised $g^{\exp}(r)$ were derived from the experimental $G^{\exp}(r)$ using equation $G(r) = 4\pi r\rho_0(\mathrm{g}(r) - 1)$ [54], in which ρ_0 refers to the number density of the structure model. Three fundamental components $g_i^*(r)$ (i = 4) were employed in the analysis. The goal of the analysis was to identify these $g_i^*(r)$ and associated weights w_{ij} (j corresponds to the number of experimental $g_j^{\exp}(r)$) to minimise $|g_j^{\mathrm{calc}}(r) - g_j^{\exp}(r)|^2$, where $g_j^{\mathrm{calc}}(r) = \sum_{i=1}^{3} w_{ij}\, g_i^*(r)$. Additional constraints were applied to ensure non-negative $g_i^*(r)$ for all i and r, and that $\sum_{i=1}^{4} w_{ij} = 1$ for all j. The initial $g_1^*(r)$ and $g_2^*(r)$ representing the known components that were fixed to respectively represent FeF_2/CuF_2 and Fe/Cu, whereas the two unknown components $g_3^*(r)$ and $g_4^*(r)$ and all w_{ij} were assigned randomly subject to the various constraints listed above. Each iteration involved random variation of these parameters, followed by the calculation of the change in $|g_j^{\mathrm{calc}}(r) - g_j^{\exp}(r)|^2$. The acceptance or rejection of the variation follows MMC algorithm. The variation was repeated under increasingly stringent acceptance criteria using simulated annealing until convergence was achieved.

Data availability

The authors declare that all data supporting the findings of this study are included within the paper and its Supplementary Information files. Source data are available from the corresponding authors upon reasonable request.

Reference:

43 Pereira, N., Badway, F., Wartelsky, M., Gunn, S. & Amatucci, G. G. Iron Oxyfluorides as High Capacity Cathode Materials for Lithium Batteries. *J. Electrochem. Soc.* **156**, A407 (2009).

44 Hammersley, A. FIT2D V9.129 reference manual V3.1. ESRF internal report 98HA01T. ESRF (1998).

45 Basham, M. *et al.* Data Analysis WorkbeNch (DAWN). *J. Synchrotron Radiat.* **22**, 853-858 (2015).

46 Qiu, X., Thompson, J. W. & Billinge, S. L. J. *J. Appl. Crystallogr.* **37**, 678 (2004).

47 Toby, B. H. & Von Dreele, R. B. GSAS-II: the genesis of a modern open-source all purpose crystallography software package. *J. Appl. Crystallogr.* **46**, 544-549 (2013).

48 Farrow, C. L. *et al.* PDFfit2 and PDFgui: computer programs for studying nanostructure in crystals. *J. Phys.: Condens. Matter* **19**, 335219 (2007).

49 Proffen, T. & Neder, R. B. DISCUS, a program for diffuse scattering and defect structure simulations - update. *J. Appl. Crystallogr.* **32**, 838-839 (1999).

50 Treacy, M. M. J., Newsam, J. M. & Deem, M. W. A General Recursion Method for Calculating Diffracted Intensities from Crystals Containing Planar Faults. *Proc. Math. Phys. Eng. Sci.* **433**, 499-520 (1991).

51 Pickard, C. J. & Needs, R. J. High-Pressure Phases of Silane. *Phys. Rev. Lett.* **97**, 045504 (2006).

52 Pickard, C. J. & Needs, R. J. Ab initiorandom structure searching. *J. Phys.: Condens. Matter* **23**, 053201 (2011).

53 Lee, D. D. & Seung, H. S. Learning the parts of objects by non-negative matrix factorization. *Nature* **401**, 788-791 (1999).

54 Egami, T. & Billinge, S. J. L. *Underneath the Bragg Peaks Structural Analysis of Complex Materials*. (Pergamon, 2012).

Acknowledgements

X.H. is supported by funding from EPSRC Doctoral Prize, Adolphe Merkle and the Swiss National Science Foundation (Program NRP70 No. 153990) and European Commission via MSCA (Grant 798169). A.S.E. acknowledges financial support from the Royal Society. E.C.M. acknowledges funding from European Commission via MSCA (Grant 747449) and RTI2018-094550-A-100 from MICINN. Z. L. acknowledges funding from the Faraday Institution via the FutureCat consortium. C.J.P. is supported by the Royal Society through a Royal Society Wolfson Research Merit award, and EPSRC grant EP/P022596/1. A.L.G. acknowledges funding from the ERC (Grant 788144). This research was supported as part of the North Eastern Center for Chemical Energy Storage, an Energy Frontier Research Center funded by the US Department of Energy, Office of Science, and Office of Basic Energy Sciences under Award Number DE-SC0001294. Work done at Argonne and use of the Advanced Photon Source, an Office of Science User Facility operated for the US Department of Energy (DOE) Office of Science by Argonne National Laboratory, was supported by the US DOE under Contract No. DE-AC02-06CH11357. Work done at Diamond Light Source was under Proposal EE17315-1. The authors are grateful to Prof. G. Ceder and other NECCES members for many stimulating discussions concerning fluoride-based conversion reactions and on the origins of structural hysteresis. The authors also acknowledge the help from S. Dutton, T. Dean, A. Docker, M. Leskes and D. Keeble.

Author contributions

X.H., E.C.M. and R.R. planned the project with C.P.G. E.C.M. and R.R. prepared the pristine materials with help from N.P. and G.G.A. X.H., E.C.M., R.R. and M.W. performed the electrochemistry tests and prepared samples for *ex situ* characterisation. E.C.M. and R.R. performed HRXRD measurements. A.S.E. acquired and analysed TEM data with support from P.A.M. X.H., R.R. and K.M.W. acquired PDF data with support from U.S. and K.W.C. X.H. performed analyses of the electrochemistry, XRD and PDF data. Z.L. and C.J.P. performed the DFT calculations. X.H., H.S.G. and A.L.G. performed the NMF analysis. X.H. and C.P.G. wrote the manuscript with the input from all the coauthors.

Corresponding author

Correspondence to Xiao Hua and Clare P. Grey.

Competing interests

The authors declare no competing interests.

Supplementary information

Sections on initial XRD refinement (S1), charge-flipping (S2), scanning electron diffraction (S3), ED analysis of *B*-$Li_xFe_yF_3$ (S4), DFT calculation (S5), SQUID magnetometry data (S6), crystal structure of C-$Li_{1+2\eta}Fe_{1-\eta}F_3$ and its lithiation (S7), charge process mechanism (S8), energy study of the interface model (S9), NMF study of lithiated CuF_2 (S10) and radiation sensitivity of FeF_x (S11), Figure S1 – S24, Table S1 – S2, Video S1 – S2 and full details on DFT computation (compressed file).

FIGURES

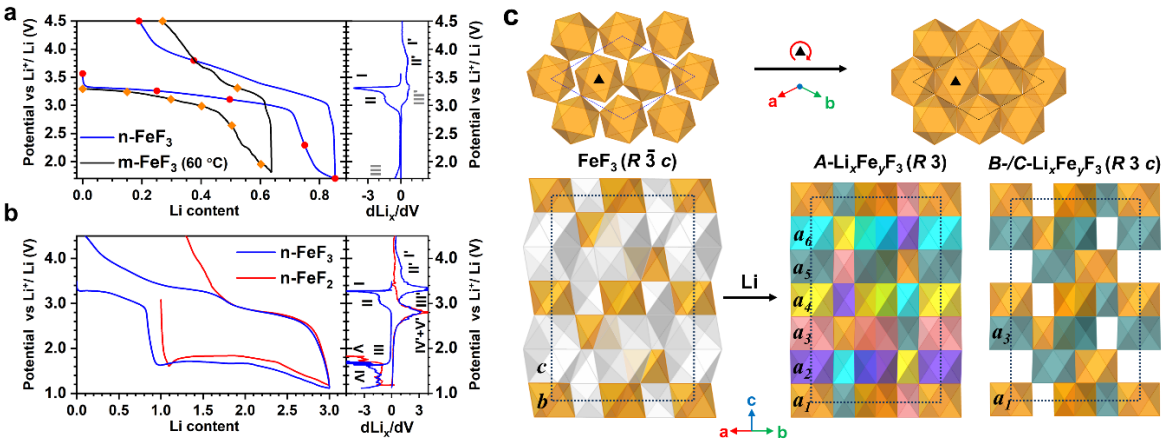

Fig. 1 | Electrochemical performance and crystal structures. Comparison of galvanostatic profiles between **a)** n-FeF_3 (blue) and m-FeF_3 (black) within the insertion cycle, and between **b)** n-FeF_3 (blue) and n-FeF_2 (red) in the full reaction cycle. The corresponding derivative curves (dLi_x/dV) from n-FeF_3 are shown with the key reactions labelled. The states of charge during the insertion cycle where X-ray scattering experiments were performed are marked. **c)** Top: projection of FeF_3 and $Li_xFe_yF_3$ along the *c*-axis. The black triangles denote a 3-fold axis around which a clockwise rotation of the FeF_6-octahedron leads to a change of anion arrangement from a slightly distorted *hcp* arrangement in FeF_3 to a near-perfect *hcp* arrangement in *A/B*-$Li_xFe_yF_3$. Bottom: structure transition from FeF_3 to the two lithiated phases, determined by HRXRD and PDF analyses. The same colours in each structure show the six equivalent [FeF_6] octahedral sites with their respective Wyckoff positions $a_1 - a_6$. The white sites in FeF_3 represents vacant sites. All Li and vertex F atoms are omitted for a clearer view.

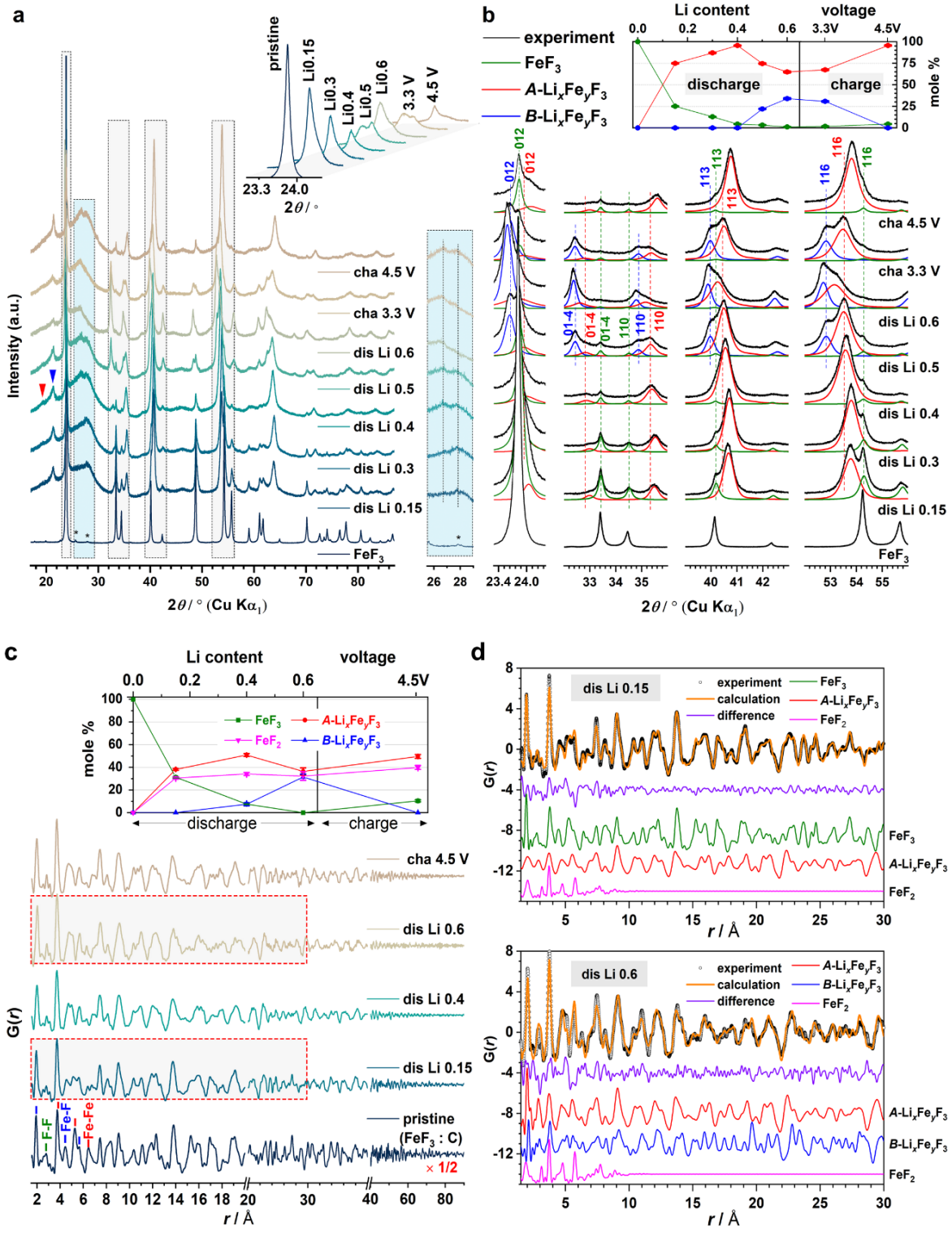

Fig. 2 | XRD and PDF analysis of m-FeF_3. a) HRXRD data for the cycled m-FeF_3 collected at selected states of charge. The (003) and (01-1) reflections of the *A*-$Li_xFe_yF_3$ phase are marked by red and blue triangles, respectively. Asterisks mark the hydrated FeF_3 impurity introduced during sample preparation. Top inset shows the intensity variations of the (012) reflection with state of charge. Right blue inset highlights the two components in the broad feature at around 26°-28° 2θ. **b)** Bragg contribution of FeF_3 (green), *A*-$Li_xFe_yF_3$ (red), and *B*-$Li_xFe_yF_3$ (blue) derived from Rietveld refinement shown in selected 2θ range. Key reflections of each phase are marked by dashed lines with indices labelled. The inset shows the evolution of the phase mole fraction within the first insertion cycle. **c)**

PDFs of m-FeF_3 collected within the insertion cycle. Low-*r* atom pairs in FeF_3 are labelled. Top inset shows the phase evolution of each component derived from refinement. The breakdown of the PDF contributions obtained from refinement of the PDFs from the red dashed rectangles are shown in **d)** where experimental, calculated and difference PDFs are shown in black circle, orange and purple lines, respectively. They are compared to the calculated PDFs from the related structures plotted using the same colour code as that in b).

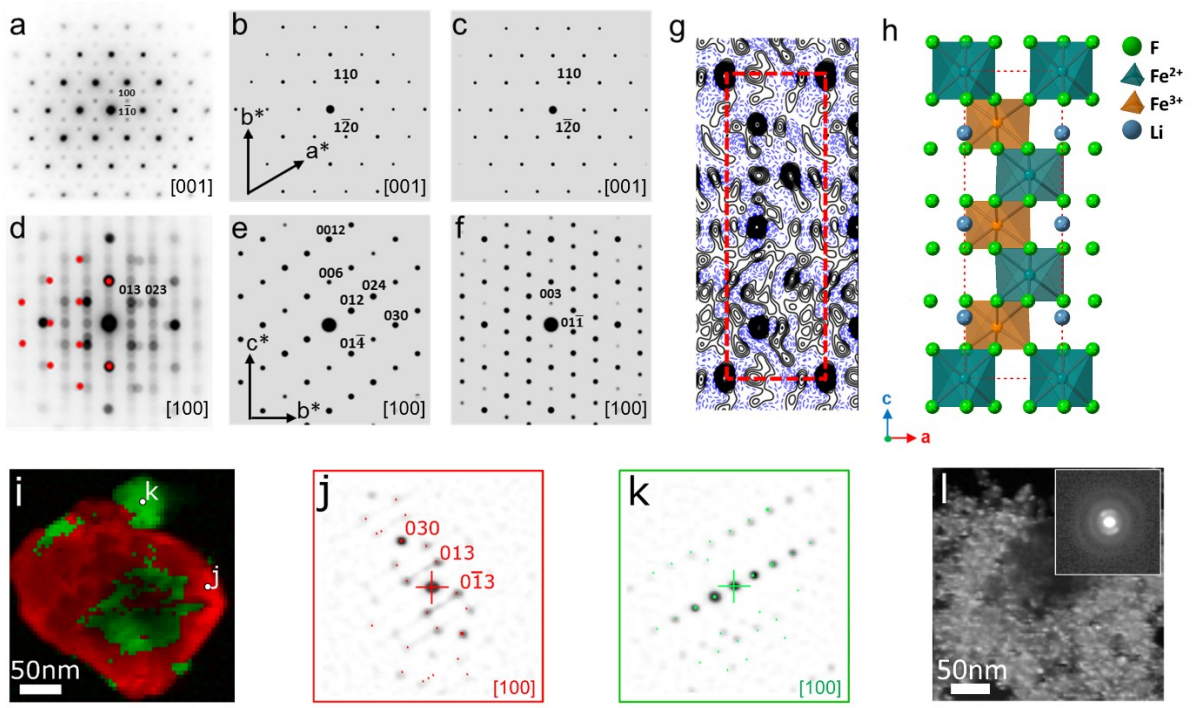

Fig. 3 | ED analyses of the partially discharged m-FeF_3 "Li 0.25" sample. a - f) Zone axis ED analysis**. a)** The diffraction pattern recorded parallel to the [001] direction of the crystal; **b)** and **c)** are simulated ED patterns for the same orientation of FeF_3 and X-ray derived *A*-$Li_xFe_yF_3$, respectively. **d)** Experimental pattern recorded parallel to [100] (additional reflections from FeF_2 in the electron beam are marked by red circles on one side of the pattern). **e)** and **f)** are simulations respectively for FeF_3 and *A*-$Li_xFe_yF_3$. **g)** A projected potential map solved from the pattern in **d)** using charge flipping. **h)** Structure model (*P*312) based on the heavy atom positions in **g)** and derived by DFT. **i)** SED analysis. The red and green colours correspond to *A*-$Li_xFe_yF_3$ and FeF_3, respectively. The diffraction pattern collected at position "j" is shown in **j)** where the strong (013)/(01-3) reflections are assigned to the *A*-$Li_xFe_yF_3$ structure. The diffraction pattern collected at position "k", **k)**, shows reflections consistent with the pristine FeF_3 structure. **l)** Direct-beam intensity mapping of the sample shows significant amounts of the less-crystalline FeF_2 phase, whose lack of long-range ordering is reflected by the diffraction pattern in the inset.

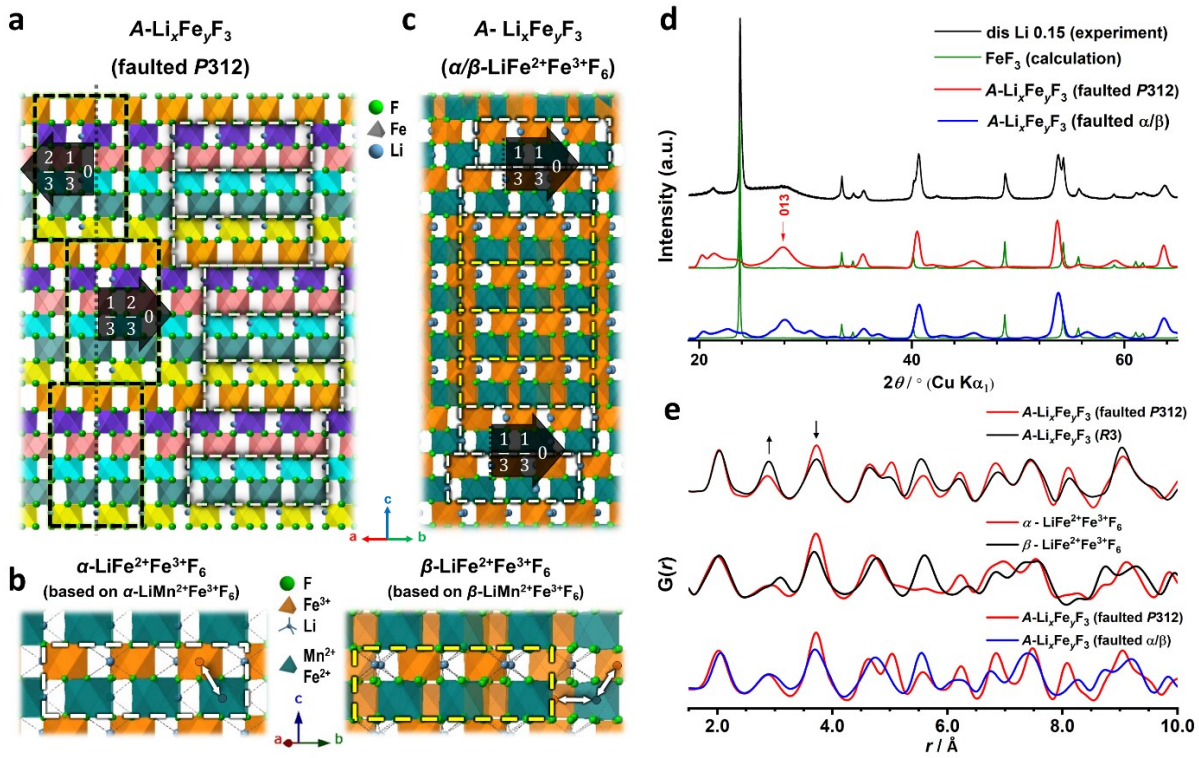

Fig. 4 | Stacking disorder in A-$Li_xFe_yF_3$. a) Faulted A-$Li_xFe_yF_3$ model constructed by stacking the ED-derived $P312$ cells (black dashed rectangles) along the c-axis with displacement vectors shown. White dashed rectangles indicate an alternative structure representation based on the $LiMnFeF_6$ structure. **b)** Structures of α-$LiFe_2F_6$ (white arrows indicate corner shared $[MF_6]$; M – Fe^{3+}, Fe^{2+} and Mn^{2+} in the related $LiM^{2+}M^{3+}F_6$ structure) and β-$LiFe_2F_6$ (white arrows indicate corner shared and edge shared $[MF_6]$). **c)** Structure of A-$Li_xFe_yF_3$ composed of disordered stacking of α- and β-$LiFe_2F_6$ units (marked by white and yellow dashed rectangle respectively) with displacement vectors indicated. **d)** XRD comparison between the experiment, calculated FeF_3 and the A-$Li_xFe_yF_3$ patterns. The A-$Li_xFe_yF_3$ patterns were simulated using the faulted model in a) and c), showing a comparable result. **e)** Top: PDF comparison between faulted $P312$ model and the average structure ($R3$) with black arrows indicating the local structure difference, which is comparable to that between α- and β-$LiFe_2F_6$ shown in the middle. Bottom: PDF comparison between simulations using the faulted models shown in a) and c).

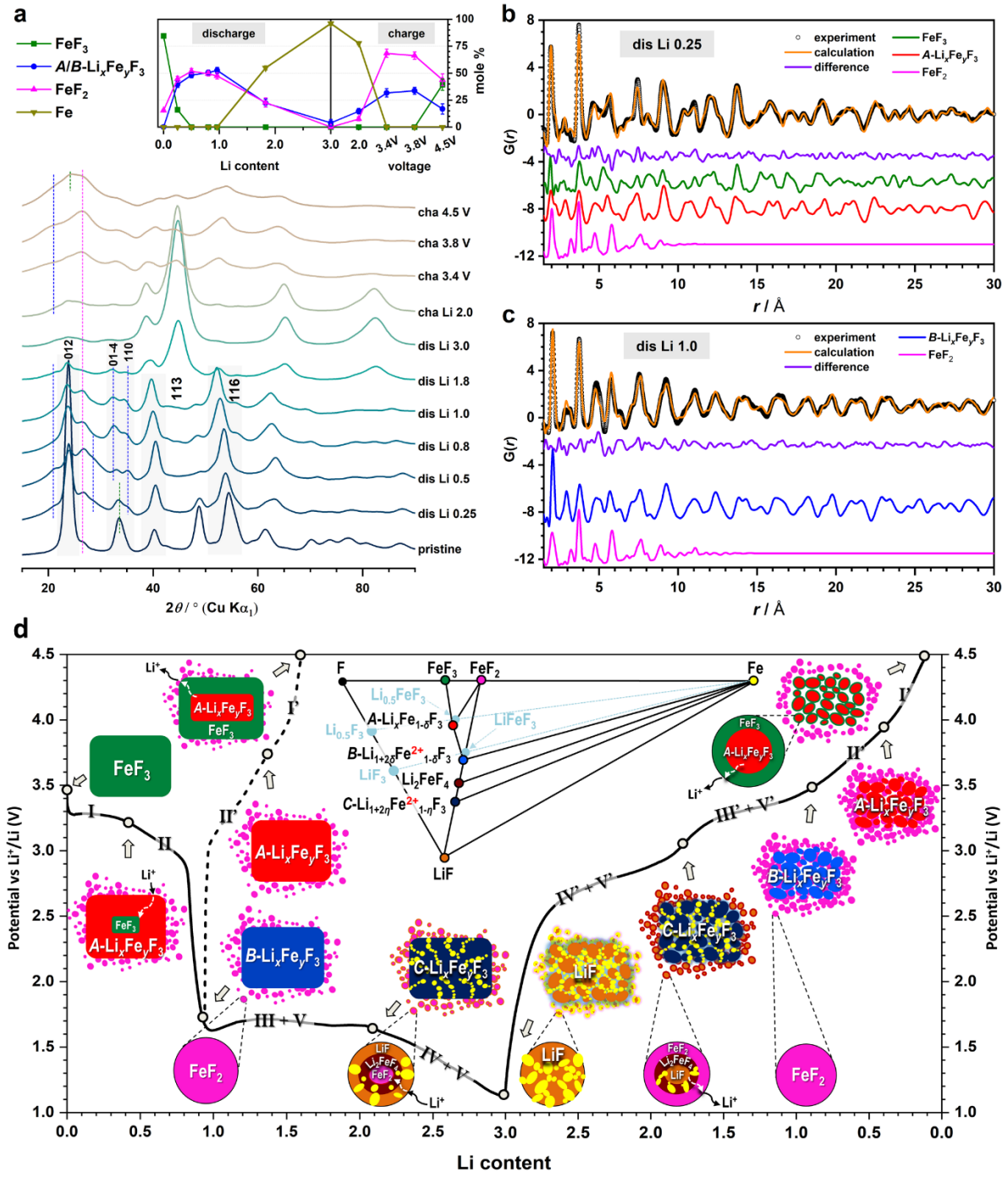

Fig. 5 | XRD and PDF of n-FeF_3 and illustrated reaction pathways for FeF_x. a) XRD data obtained from X-ray total scattering experiment of selected n-FeF_3 samples. Structural features that highlight the similarity with the data obtained for m-FeF_3 in Fig. 2a are shaded and indexed. Bragg peaks unique to FeF_3 (green), *A*/*B*-$Li_xF_yF_3$(blue), FeF_2 (pink) and Fe (dark yellow) are marked by dotted lines. Inset shows phase evolution of these phases derived from refinement of the corresponding PDF data. The presence of FeF_2 in the pristine sample results from the reduction of FeF_3 via ball-milling, during which carbon is fluorinated to form CF_x[41]. The refinement results of **b)** "dis Li 0.25" and **c)** "dis Li 1.0" n-FeF_3 are broken down into the patterns from the individual phases to highlight the similar phase behaviour seen during lithiation for n- and m-FeF_3 (latter shown in Fig. 2d). **d)** Simplified Li-Fe-F ternary phase diagram (see Extended Data Fig. 2 for the full diagram) and illustration of reaction pathways of the FeF_3-FeF_2 system (with voltage curves for insertion charge and full reaction cycle

respectively denoted using dashed and solid lines). The reference phases in the phase diagram are labelled and indicated by light blue circles to indicate the positions of the *A*- and *B*-$Li_xFe_yF_3$, whose Fe concentration is off-stoichiometric. The colour of each phase in the phase diagram is consistent with those in the pathway illustration. Impeded internal and external Li transport is indicated by black solid and white dashed arrows, respectively.

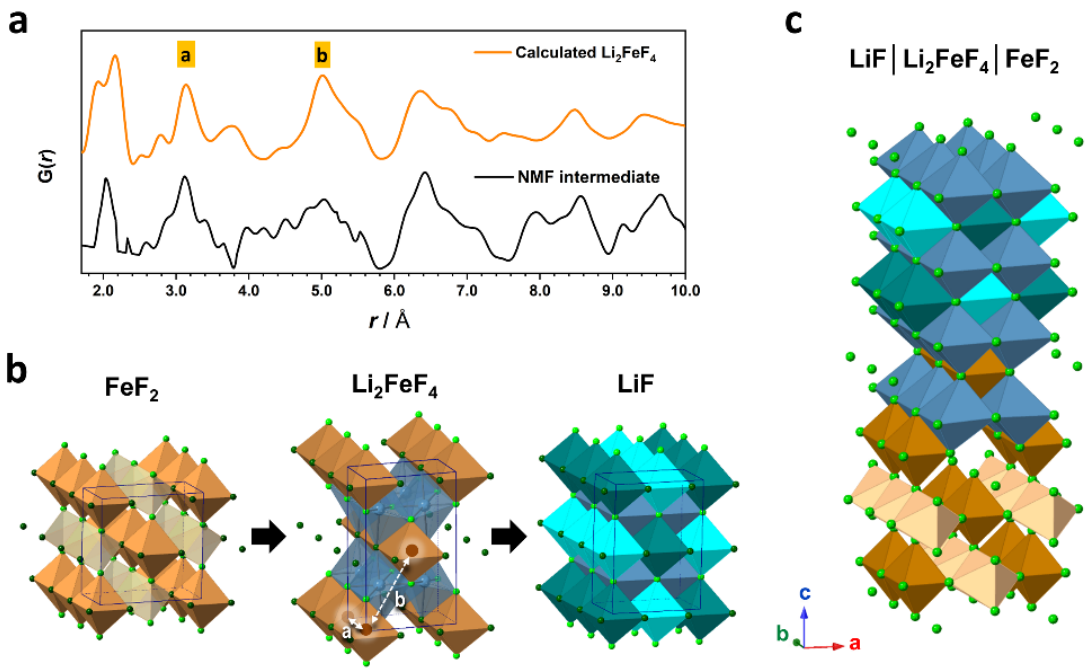

Fig. 6 | Formation of interfacial intermediate upon lithiation of FeF_2. a) PDF comparison between the calculated pattern and the NMF-derived pattern for Li_2FeF_4 (*Cmmm*). **b)** The structures of the reactant (FeF_2), intermediate (Li_2FeF_4) and product (LiF). To highlight a topological relationship between these phases, these structures are represented by using the unit cell and symmetry setting of Li_2FeF_4. In each phase, the atoms that are equivalent based on the *Cmmm* symmetry are depicted using the same colour. The two unique Fe-Fe atom pairs in Li_2FeF_4 are indicated by "a" and "b" in the structure and PDF pattern. **c)** "LiF|Li_2FeF_4|FeF_2" interface model, which contains an interfacial Li_2FeF_4 block coherently connected to LiF and FeF_2 units based on their symmetry relationships, shown using the same colour code used in b).

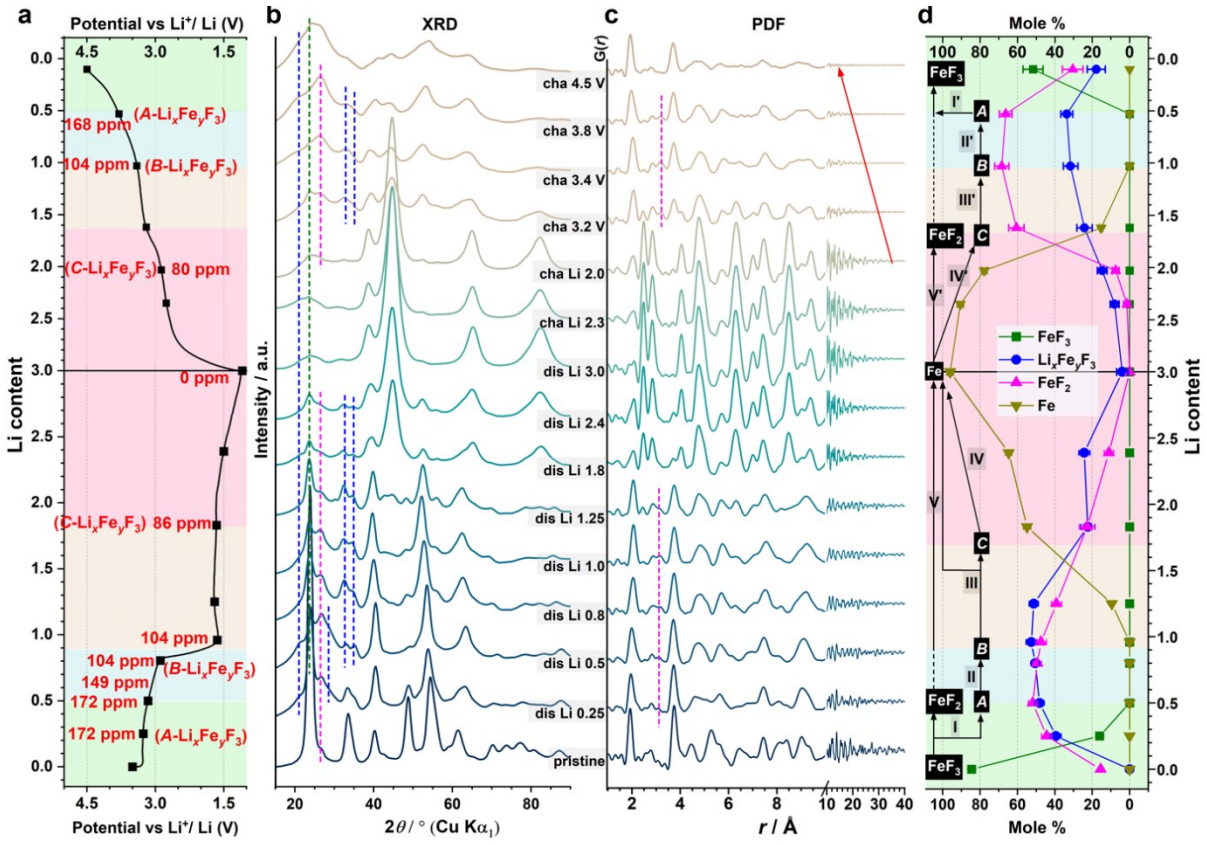

Extended Data Fig. 1 | NMR, XRD and PDF results of n-FeF_3 in the first cycle. a) Galvanostatic profile of n-FeF_3's first cycle with distinct reaction processes indicated by different colour backgrounds. The ^{6}Li MAS NMR chemical shifts (red) from our previous study[10] are labelled at their respective state of charge with the main phase identification indicated. Black squares mark the states of charge where *ex situ* X-ray total scattering experiments were performed to acquire **b)** XRD and **c)** PDF patterns. Green, blue and pink dotted lines indicate unique Bragg or PDF features from FeF_3, $Li_xFe_yF_3$ and FeF_2, respectively. The red arrow highlights a drastic decrease in the samples' particle sizes upon charge. The evolution of the phase mole fractions obtained from the PDF refinement is shown in **d)** with the deduced step-by-step mechanism diagram indicated on the left, which echoes with the simplified scheme shown in Fig. 5d.

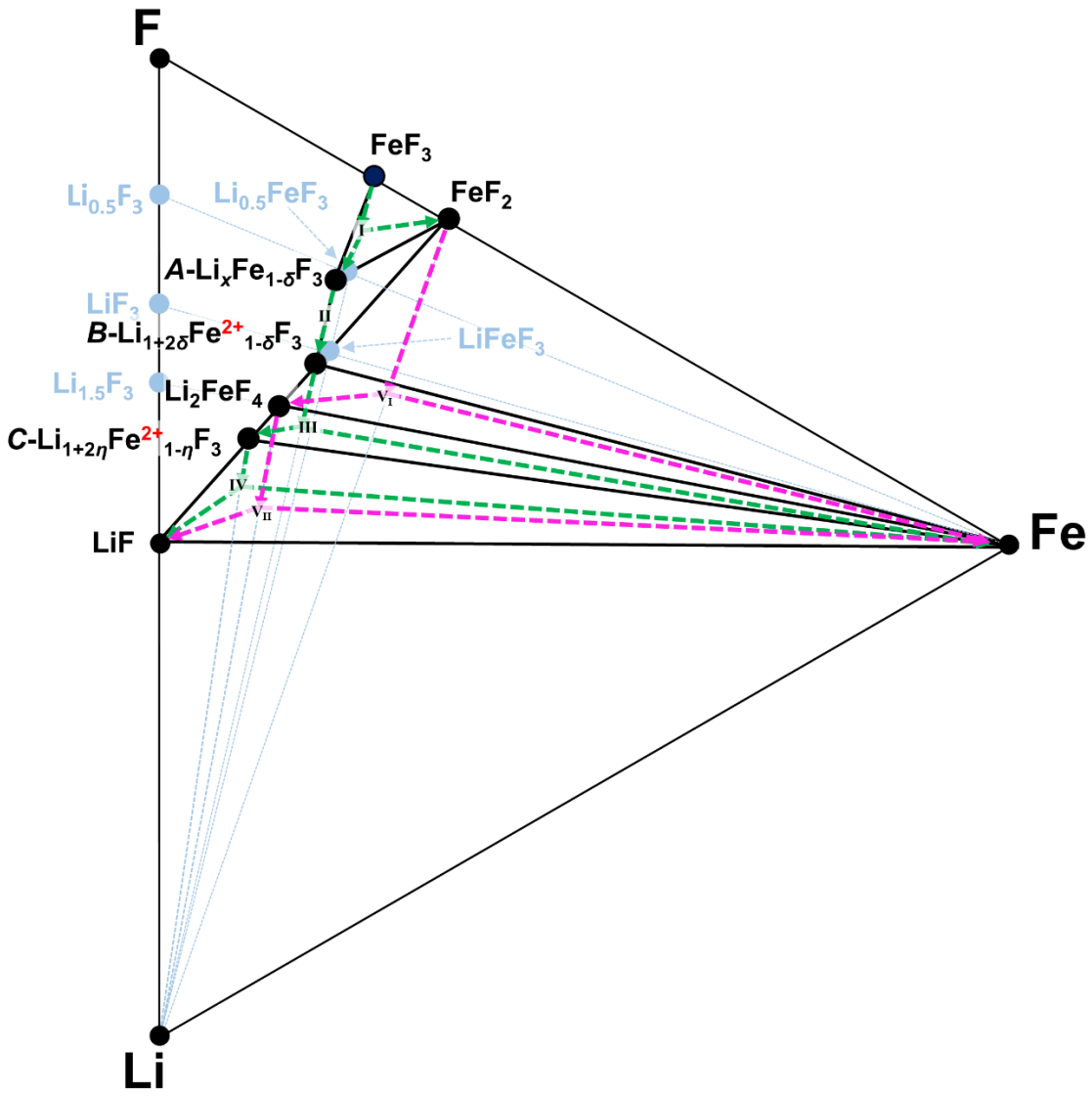

Extended Data Fig. 2 | Li-Fe-F phase diagram. The reference phases in the phase diagram are labelled and indicated by light blue circles so as to indicate the positions of *A*- and *B*-$Li_xFe_yF_3$, whose Fe concentration is off-stoichiometric. The reaction pathways associated with the FeF_3 and FeF_2 systems are respectively marked by using green and pink dashed arrows. Each reaction process is also labelled with its respective roman numeral used to label the equations in the manuscript.